Catalysis Science & Technology

ROYAL SOCIETY OF CHEMISTRY

PAPER

View Article Online
View Journal | View Issue



Cite this: *Catal. Sci. Technol.*, 2022, 12, 3311

# Theoretical investigation of the olefin cycle in H-SSZ-13 for the ethanol-to-olefins process using *ab initio* calculations and kinetic modeling†

Jonas Amsler, [a] Sarah Bernart, [a] Philipp N. Plessow *[a] and Felix Studt [ab]

The formation of the hydrocarbon pool (HCP) in the ethanol-to-olefins (ETO) process catalyzed by H-SSZ-13 is studied in a kinetic model with *ab initio* computed reaction barriers. Free energy barriers are computed using density functional theory (DFT) and post-Hartree–Fock methods with a complete basis set extrapolation applied to a hierarchy of periodic and cluster models. The kinetic model includes ethanol (EtOH) dehydration to ethene as well as olefin ethylations up to hexene isomers and the corresponding cracking reactions. Ethylation of ethene and of products thereof leads only to even-numbered olefins, while cracking can lead to propene and thus initiate the formation of olefins with an odd number of carbon atoms. During EtOH dehydration at 473.15 K we observe diethyl ether (DEE) formation for a short period of time where the DEE selectivity decreases monotonically with increasing EtOH conversion. At 673.15 K we find that EtOH dehydration occurs much faster than ethylation of the formed ethene, which takes considerably longer due to higher free energy barriers. Hexene isomers form on the same time scale as butene, where branched isomers are favored with 2-methyl-pentene isomers contributing most to the formation of propene through cracking. As in the methanol-to-olefins (MTO) process, the most relevant alkylation pathway is the stepwise mechanism *via* surface alkoxy species (SAS) on the zeolite catalyst. A comparison of ethylation with methylation barriers of up to heptene isomers forming nonene and octene isomers, respectively, shows that ethylation barriers are lower by around 11 kJ mol$^{-1}$ on average.

Received 17th December 2021,
Accepted 4th April 2022

DOI: 10.1039/d1cy02289j

rsc.li/catalysis



## 1 Introduction

The zeolite-catalyzed ethanol-to-olefins (ETO) process and its closely related methanol-to-olefins (MTO) process are promising key drivers in the value-added chain from biomass to fuels and raw materials for the petrochemical industry partaking in a sustainable energy economy.[1,2] Aided by crystalline microporous zeolite catalysts at temperatures around 673 K to 823 K and intermediate pressures around 1 bar to 5 bar, ethanol (EtOH) and methanol (MeOH) are converted into light olefins in these processes.[3] The current understanding of the mechanistic details revolves around the concept of the hydrocarbon pool (HCP) comprised of a variety of (unsaturated) hydrocarbons that continuously undergo oligomerization and cracking reactions.[4–10] While the initial formation of carbon–carbon bonds in the multi-step initiation of the MTO process from MeOH has been attributed to either impurities[11–14] or direct initiation,[15–18] the ETO process initiates *via* EtOH dehydration to ethene.[19] In a majority of experimental studies, the ETO conversion was performed on (modified) H-ZSM-5 where the first stage of EtOH dehydration proceeds at a high rate and is virtually independent of the selectivity of the catalyst towards higher olefins.[2] The most important acid-catalyzed reactions (dehydration, alkylation/oligomerization, isomerization, cyclization, aromatization, hydrogen transfers and cracking) in the HCP are promoted by the acidic Brønsted sites and governed by the structural properties (framework, pore size) as well as the acidity of the catalyst.[20]

Several studies have compared different zeolites and have demonstrated excellent activity in the dehydration reaction of EtOH to ethene,[21] and further reactions to a complex mixture of short-chain hydrocarbons.[22,23] In the experimentally determined thermodynamic equilibrium between EtOH, diethyl ether (DEE) and ethene at atmospheric pressure the ratio of DEE : ethene is 1 : 1 at roughly 370 K, while above 450 K no significant amount of DEE is observed.[24] However, in many experimental studies the actually observed product ratio greatly varies with the overall reaction conditions,[25] such as EtOH pressure,[26] catalyst contact time, overall conversion and temperature. A particularly high sensitivity of the ethene selectivity to the catalyst contact time

[a] *Institute of Catalysis Research and Technology, Karlsruhe Institute of Technology, Hermann-von-Helmholtz-Platz 1, 76344 Eggenstein-Leopoldshafen, Germany. E-mail: plessow@kit.edu*
[b] *Institute for Chemical Technology and Polymer Chemistry, Karlsruhe Institute of Technology, Kaiserstr. 12, 76131 Karlsruhe, Germany*

† Electronic supplementary information (ESI) available: Computational details, energies for all involved species. Structure coordinates. See DOI: https://doi.org/10.1039/d1cy02289j

and temperature has been found in H-SAPO-34 in the narrow temperature interval from 458 K to 503 K.[27] Many other experimental works have been reported.[25] Tong used a diluted EtOH solution (20%) over H-ZSM-5 and achieved 99% conversion with 80% ethene selectivity at 672 K, and 42% conversion with 72% ethene selectivity at 571 K.[28] Le Van Mao *et al.* observed 96% conversion of EtOH solution (15%) over H-ZSM-5 at 673 K with 49% ethene selectivity.[29] Phillips and Datta applied EtOH in very low pressures and discovered that temperatures below 473 K are too low for EtOH dehydration leading to catalyst deactivation.[30] Pan and Li used modified H-ZSM-5 at 533 K and obtained 98% conversion with 98% to 99% ethene selectivity.[31,32] Wang *et al.* fed 0.2 MPa EtOH, water and Ar carrier gas to H-SAPO-34 at 493 K to 593 K where the observed EtOH conversion was 90% with an ethene selectivity of 99% above 533 K, whereas DEE was generated at lower temperatures.[33] Zhou *et al.* used 0.1 MPa EtOH at 513 K over H-SAPO-11/H-ZSM-5 to achieve a conversion of 99% with 99% ethene selectivity.[34] Xin *et al.* used H-ZSM-5 at 1 atm and 473 K with an EtOH partial pressure of 19.8 kPa diluted in He. The observed conversion was around 70% to 76% with ethene selectivities ranging from 5% to 17% depending on the degree of dealumination and desilication of the catalyst tuning its acidity for controlled selectivity.[35] Phung *et al.* compared FER, MFI, MOR, BEA, Y, and USY catalysts using a feed of 7.9% EtOH in $N_2$ carrier gas to observe over 70% DEE at 473 K with MFI and BEA, 99.9% ethene selectivity at 573 K with FER and FAU/USY (competition with DEE was not relevant under practical conditions). Confinement was concluded to explain the observations best. EtOH conversion occurred only above 400 K with almost full conversion at temperatures above 600 K. DEE was the main product at low temperatures and low conversion but decreased at 500 K.[36] Zhang *et al.* found that 90% EtOH conversion and 90% ethene selectivity can be achieved with zeolite catalysts or catalytically active $Al_2O_3$ but the latter requires higher temperatures by at least 100 K. Among zeolites, the required temperature for similar conversion and ethene selectivity can differ by up to 70 K.[21] In tests with heteropoly acids it was concluded that DEE and ethene are probably produced mostly through parallel routes rather than following a consecutive reaction scheme.[37,38] In a theoretical study using H-ZSM-5, however, Alexopoulos *et al.* identified the consecutive dimer-mediated etherification followed by ether decomposition to be energetically most favorable for EtOH dehydration to ethene at 500 K – closely followed by the ethoxide-mediated mechanism.[26] EtOH conversion and ethene selectivity thus strongly depend on the employed catalyst and the reaction conditions.[22]

Chowdhury *et al.* have elucidated the homologation reaction network originating from ethene with homologated and non-homologated products.[10] In the absence of methylation reactions, the ETO reaction network can thus be thought of two separate networks for the even and odd-numbered olefins, interconnected by cracking reactions, see Scheme 1. This concept of even and odd-numbered carbon units is further supported by Ingram and Lancashire who found that propene formation mainly originates from cracking of hexene isomers.[39]

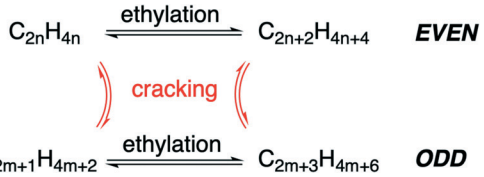


**Scheme 1** Concept of dividing the HCP into the even and the odd-numbered olefins self-contained through ethylations but partially interconnected by cracking reactions ($n, m \in \mathbb{N}$).

Quantum chemical calculations, typically based on density functional theory (DFT) are nowadays routinely used to study the reaction mechanisms associated with *e.g.* the HCP cycle. These methods are able to predict reaction barriers thus shedding light on reaction mechanisms and determining possible rate determining steps. Often, the obtained data also serves as input for (micro)kinetic models of the corresponding processes.[40–49] For instance, Alexopoulos *et al.* have shown that a reaction path analysis of EtOH dehydration from free energy profiles should include the effect of reaction conditions, feed concentrations and conversion levels. While DFT and *ab initio* post-Hartree–Fock (HF) calculations have been used extensively for MTO and related processes,[13,14,41,45,48,50–55] theoretical insight into the analogous conversion of EtOH in acidic zeolites has so far mostly been limited to EtOH dehydration to ethene and DEE[26,56–58] and is rather scarce for subsequent propagation steps.

Herein we use a hierarchical approach employing periodic DFT (PBE-D3) calculations to periodic models corrected by highly accurate post-HF (DLPNO-CCSD(T)) calculations on cluster models.[59] This way, the periodic DFT calculations take the steric implications of the entire zeolite framework into account while the high-level post-HF method yields accurate electronic energies.[55,60,61] The calculated reaction barriers serve as input for a microkinetic model comprising EtOH dehydration in competition with diethyl ether (DEE) formation as well as subsequent ethylation and cracking reactions up to hexene isomers. We furthermore compare stepwise ethylation barriers with methylation barriers studied previously for the MTO process.

## 2 Results and discussion

This work is divided into three parts. We start by investigating the conversion of ethanol (EtOH) to diethyl ether (DEE) and ethene. Subsequently, we show our results regarding the ethylation of ethene to butene and further formation of hexene as well as the selectivities among hexene isomers. Lastly, we discuss similarities and differences of EtOH conversion with the well-established MTO process.

### 2.1 Conversion of EtOH to DEE and ethene

We computed stepwise and concerted reaction pathways for the conversion of EtOH to DEE and ethene as depicted in the

 

reaction scheme in Fig. 1a. EtOH dehydration to DEE or ethene starts by adsorption of EtOH at the acid site of H-SSZ-13, for which we computed a Gibbs free energy of adsorption of −12 kJ mol$^{-1}$ and 23 kJ mol$^{-1}$ for temperatures of 473.15 K and 673.15 K, respectively. Starting from adsorbed EtOH (ZOH*EtOH), the reaction network for the formation of DEE comprises both the stepwise (gray and green lines) and concerted (orange line) mechanisms. Due to a high barrier for direct DEE decomposition on H-SSZ-13 (red line), the stepwise dehydration mechanism has lower overall free energy barriers, already at 473.15 K. At 673.15 K, the stepwise barriers are 131 kJ mol$^{-1}$ and 125 kJ mol$^{-1}$ when measured from adsorbed EtOH. Ethene formation can occur *via* three different mechanisms, namely *via* (1) direct dehydration of adsorbed EtOH (blue line), (2) the dehydration of adsorbed DEE (red line) and (3) from surface ethoxy species (SES), whereby the acid site is reestablished again (black line). At 673.15 K these barriers have values of 175 kJ mol$^{-1}$, 168 kJ mol$^{-1}$, and 125 kJ mol$^{-1}$, when referenced to adsorbed EtOH, adsorbed DEE and SES, respectively. Judging from the calculated Gibbs free energy diagram in Fig. 1b at 673.15 K, the stepwise mechanism (formation of SES and subsequent elimination to ethene (gray and black lines)) has the overall lowest barriers for ethene formation (154 kJ mol$^{-1}$ and 131 kJ mol$^{-1}$ when referenced to EtOH in the gas phase and adsorbed at the acid site, respectively). We observe, however, that the ranking of the barriers for DEE and ethene formation (green and black lines) changes with temperature. In consequence, at 473.15 K DEE formation is kinetically favored before the thermodynamically slightly more stable ethene eventually dominates the gas phase composition upon higher conversions (the chemical equilibrium between EtOH, DEE and ethene depends strongly on the temperature, see Fig. S2 in the ESI† and Garbarino *et al.*[24]). Thus, we can use this finding to explain why the conversion-dependent formation of DEE decreases with increasing temperature.

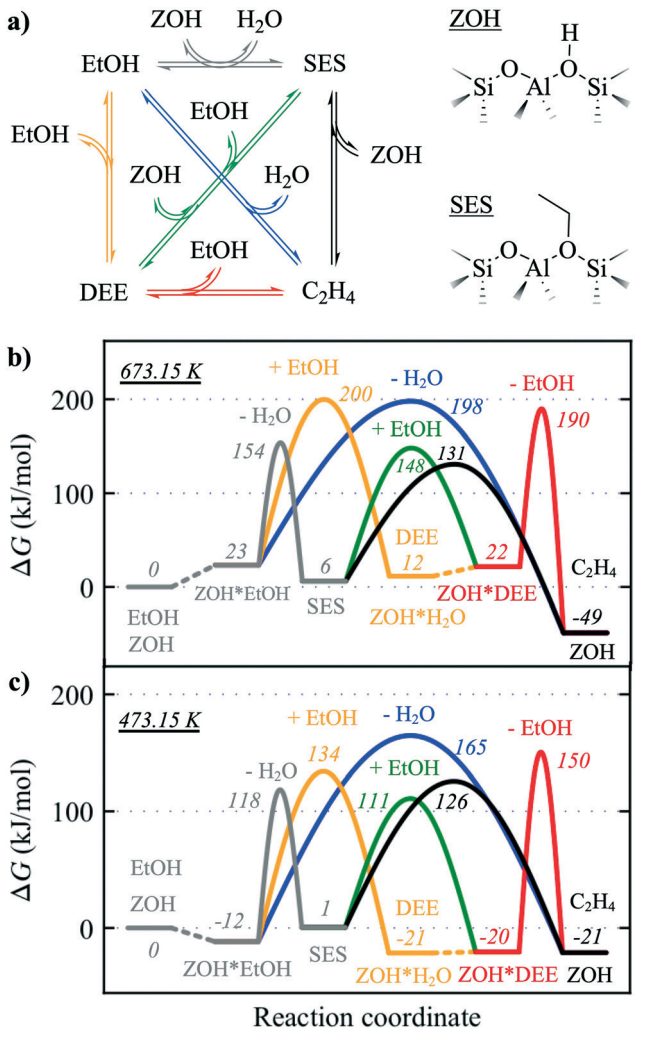


**Fig. 1** Reaction scheme for a) EtOH dehydration pathways with corresponding calculated Gibbs free energy diagrams for the conversion of ethanol (EtOH) to diethyl ether (DEE) and ethene in H-SSZ-13 at pressures of 1 bar for a temperature of b) 673.15 K and c) 473.15 K.

In order to shed more light on the formation of DEE and ethene and to identify reaction pathways, we also performed simulations of the kinetics using a batch reactor model with the reaction scheme shown in Fig. 1a. The barriers at 673.15 K for the kinetic model are summarized in Table 1 and the data at 473.15 K and 573.15 K are listed in Tables S1 and S2 of the ESI.† Fig. 2 shows the outcome of the kinetic simulations using a feed of 1 bar EtOH and three different temperatures. The upper panel of Fig. 2 shows simulated partial pressures, while the coverages of all possible intermediates are given in the lower panel.

Note that due to our choice of initial settings, surface coverage corresponds equally to partial pressure (a DEE coverage of 0.15 corresponds to 0.15 bar DEE when desorbed). As expected, surface coverages decrease with increasing temperatures where adsorbed water dominates among the surface species. At 473.15 K, DEE is the dominating product during the first minute where half of the amount of DEE is adsorbed at the reactive centers. Our simulations predict a theoretical initial DEE selectivity ($S$) of

**Table 1** Adsorption free energies of water, EtOH and DEE as well as forward and backward free energy barriers at 673.15 K and pressures of 1 bar for all elementary reaction steps shown in Fig. 1a

| No. | Elementary reaction | | $\Delta G^{\ddagger}\left(\frac{\text{kJ}}{\text{mol}}\right)$ |
|---|---|---|---|
| 1 | ZOH + $H_2O$ | ⇄ZOH*$H_2O$ | 25[a] |
| 2 | ZOH + EtOH | ⇄ZOH*EtOH | 23[a] |
| 3 | ZOH + DEE | ⇄ZOH*DEE | 35[a] |
| 4 | ZOH*EtOH | ⇄SES + $H_2O$ | 131, 148 |
| 5 | SES + EtOH | ⇄ZOH*DEE | 142, 127 |
| 6 | ZOH*EtOH + EtOH | ⇄ZOH*$H_2O$ + DEE | 176, 188 |
| 7 | SES | ⇄ZOH + ethene | 125, 180 |
| 8 | ZOH*EtOH | ⇄ZOH*$H_2O$ + ethene | 175, 222 |
| 9 | ZOH*DEE | ⇄ZOH*EtOH + ethene | 168, 215 |

[a] Adsorption free energies; low thermodynamically consistent barriers have been used for numerical reasons with no rate-limiting effect to the simulation results, see Fig. S1 in the ESI.†

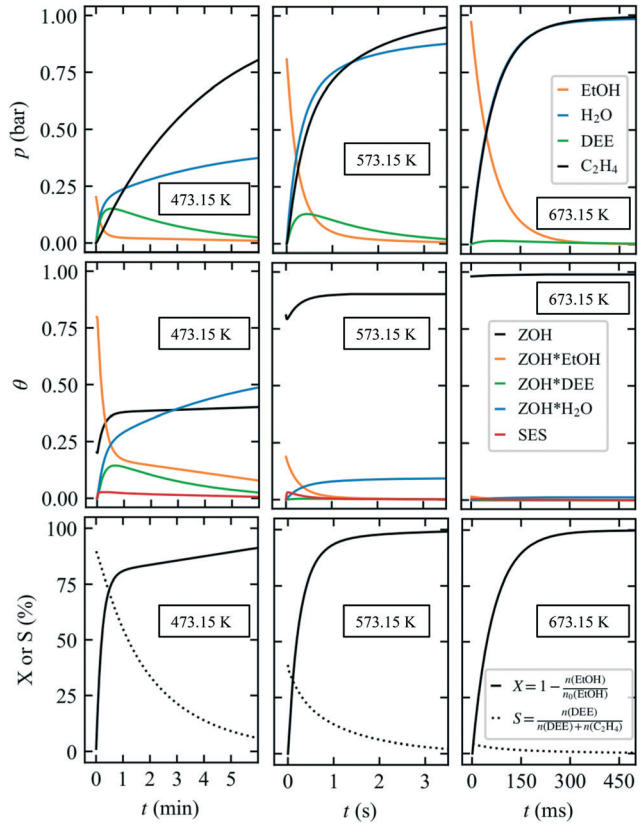


Fig. 2 Simulated partial pressures of gas phase species (top row), surface coverages (middle row) as well as EtOH conversion ($X$) and selectivity ($S$) of DEE (bottom row) at three different temperatures as a function of time using the reaction mechanism shown in Fig. 1a with data shown in Table 1 and an initial pressure of 1 bar EtOH. Note that the time scale differs significantly, being minutes (473.15 K), seconds (573.15 K) and milliseconds (673.15 K).

90% at 0.2% conversion which decreases monotonically with increasing EtOH conversion ($X$). After 50 s at 473.15 K we observe a peak DEE yield with a DEE selectivity of 61% and an EtOH conversion of 79%. At 673.15 K on the other hand, ethene is simulated to form within hundreds of ms, while DEE is not present in large amounts throughout the simulation time. This behavior depending on temperature and conversion can be understood by the temperature-dependent ranking of the barriers for DEE and ethene formation, as discussed above. We also note that the absence of DEE formation at elevated temperatures is in line with experimental observations.[24,27,31–34,36,62] Besides the temperature dependence, we also observe conversion to be significant for DEE and ethene selectivity. After one minute at 473.15 K, 81% of the EtOH have been converted into DEE (56%) and ethene (25%) on a per carbon basis. At higher conversion and for longer reaction times, ethene becomes the dominant product since the thermodynamic equilibrium favors ethene even at 473.15 K (see ESI†). A high variation of the ethene selectivity within a narrow temperature range and depending on the catalyst contact time was also reported for EtOH dehydration in H-SAPO-34 by Potter *et al.*[27] At 473.15 K and a contact time of 22 min they observed 40 mol% DEE and 10 mol% ethene. Moreover, ethene increased to 20 mol% when the contact time increased to 90 min. At 503.15 K, their measured ethene selectivity went up to 45 mol% and 80 mol% for the same contact times of 22 min and 90 min, respectively. H-SSZ-13 and H-SAPO-34 exhibit the same CHA topology with a pore size of 3.7 Å and virtually identical van-der-Waals (vdW) interactions.[63] From the higher acidity of H-SSZ-13 we expect slightly lower barriers (higher rates) in our case with, nevertheless, a similar effect of temperature. In MTO experiments, H-SSZ-13 displayed a higher conversion capacity at lower temperatures.[64]

Our kinetic simulations thus show that DEE selectivity varies greatly with temperature, conversion and catalyst contact time, with DEE being mainly observed at lower temperature and lower conversion.

### 2.2 Ethylation of olefins

In this section, we focus on a small subset of the ETO reaction network comprising only olefins with an even number of carbon atoms as well as their cracking products (including propene). The alkylation pathways shown in Scheme 2 are inspired by the methylation pathways in the methanol-to-olefins (MTO) process.[50] We consider stepwise and concerted mechanisms, in other words, the formation of surface ethoxy species (SES) followed by a reaction with an olefin and the direct reaction of the olefin with an alkylation agent (EtOH, DEE, or ethene) at the acid site.

**2.2.1 Ethylation of ethene to butene.** After ethene formation from EtOH, the route to higher olefins necessarily proceeds *via* ethylation of ethene.[19] As mentioned above, we always consider ethylation pathways through the three ethylation agents (EtOH, DEE and SES) and potentially further ethylation pathways by olefin dimerization. Butene formation from ethene can thus proceed *via* the four reactions listed in Table 2. From the listed intrinsic free energy barriers, the lowest barrier of 173 kJ mol$^{-1}$ is found for ethylation by SES formed from ethene (at 673.15 K). Note that the lowest ethylation barrier is still significantly higher than the lowest barrier for ethene formation from SES with 125 kJ mol$^{-1}$. We thus conclude that the conversion of EtOH to ethene is much faster than the subsequent butene

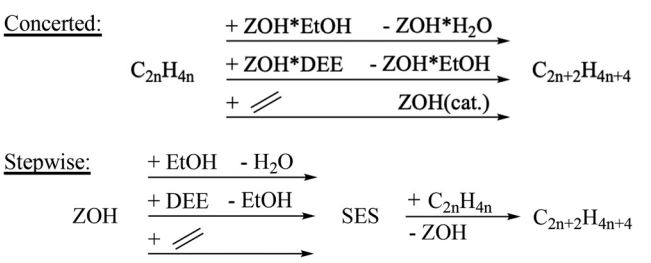


Scheme 2 Depiction of stepwise and concerted ethylation paths.

**Table 2** Elementary reaction steps for the formation and cracking of butene with forward and backward free energy barriers at 673.15 K

| No. | Elementary reaction | | $\Delta G^{\ddagger}\left(\frac{\text{kJ}}{\text{mol}}\right)$ |
|---|---|---|---|
| 10 | ZOH*EtOH + ethene | ⇄ZOH*$H_2O$ + butene | 205, 274 |
| 11 | SES + ethene | ⇄ZOH + butene | 173, 250 |
| 12 | ZOH*DEE + ethene | ⇄ZOH*EtOH + butene | 199, 267 |
| 13 | ZOH + 2 ethene | ⇄ZOH + butene | 250, 272 |

formation. Unsurprisingly, the intrinsic formation/cracking barrier for the short-chained butene is very high in both directions (250 kJ $mol^{-1}$ and 272 kJ $mol^{-1}$).[65,66] The Gibbs free energy diagrams corresponding to stepwise and concerted butene formation and cracking at 673.15 K along with optimized transition structures are shown in Fig. 3. Inspection of Fig. 3 shows that the intrinsic barrier for the SES-mediated dimerization of ethene is higher in comparison to the reactions of ethene with EtOH or DEE. Thermodynamically, however, ethene is considerably lower in free energy than DEE or EtOH (see Fig. S3 in the ESI†), such that the ethene dimerization to butene *via* SES (see Fig. 3c) is actually the most favorable pathway from a kinetic point of view. In addition, since ethene is formed rapidly, see Fig. 2, the partial pressure of ethene will be much higher than that of either EtOH or DEE. We thus conclude, that the overall lowest ethylation barrier is found for the stepwise ethylation pathway *via* SES.

**2.2.2 Formation of hexene isomers.** Ethylation from butene onwards can lead to a variety of hexene isomers. The Gibbs free energy diagrams for the corresponding ethylation, cracking and methyl shift reactions are shown in Fig. 4. Analogous to the ethylation of ethene, the overall lowest ethylation barrier of butene is found for the stepwise ethylation by SES formed from ethene (black barriers in Fig. 4c), followed by ethene dimerization (red barrier in Fig. 4c), direct ethylation through DEE and direct ethylation with EtOH. Hence, our calculations indicate that the preferred alkylation pathway in the ETO process is similar to that identified for the MTO process, that is alkylation *via* surface alkoxy species (SAS) in the stepwise pathway. A comparison of the ethylation pathways towards linear and branched hexene isomers shows that the formation of branched products is favored with lower barriers and more favorable reaction energies which principally obeys the idea of the Brønsted–Evans–Polanyi (BEP) principle. For analogous stepwise methylations of olefins by MeOH this BEP principle, which relates energy barriers with reaction energies, has been applied in the literature to estimate barriers from reaction energies.[67,68] The preference of branched products over linear products can also generally be observed, as we will also see later on in section 2.3. In particular, the stepwise ethylation barrier for the formation of 3-methyl-pentene is by 19 kJ $mol^{-1}$ lower than the analogous formation of hexene. Relative to ethene in the gas phase the free energy barriers for the

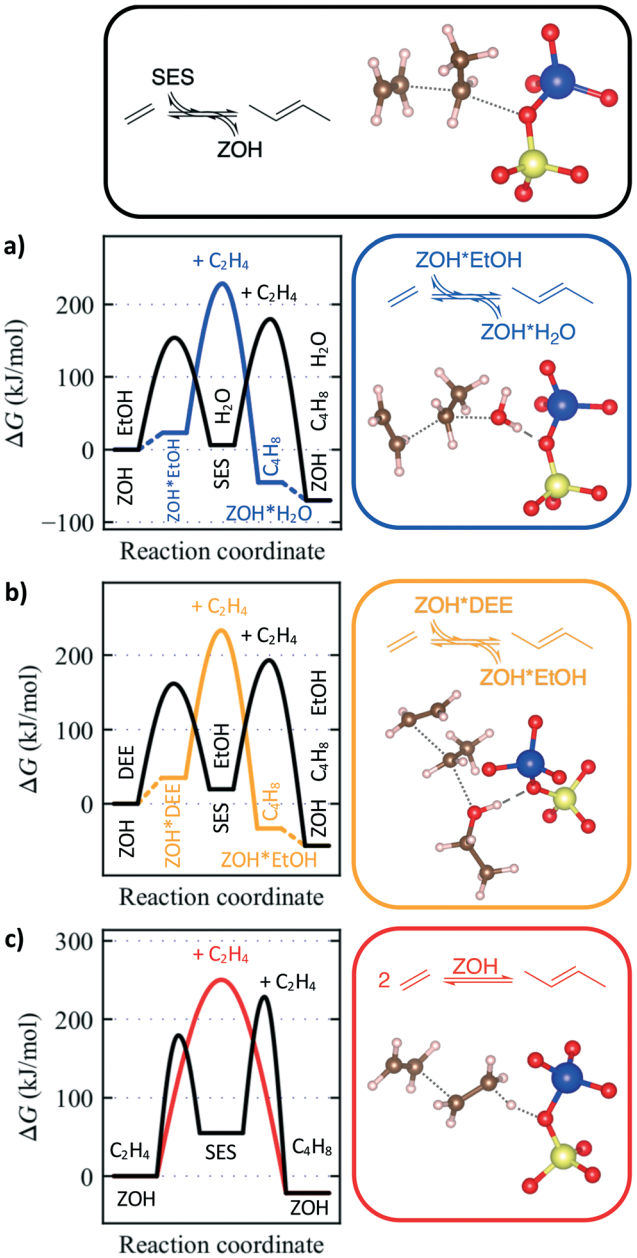


**Fig. 3** Gibbs free energy diagram and transition structures for the direct ethylations of ethene at 673.15 K through a) EtOH (blue), b) DEE (orange) and c) ethene (red). Corresponding stepwise ethylations are shown in black.

methyl shift of 3-methyl-pentene to 2-methyl-pentene and subsequent cracking to propene are slightly lower than the formation of 3-methyl-pentene from ethene and butene (see Fig. S4 in the ESI†). Once longer olefins are formed, the formation of propene and subsequent formation of other odd-numbered olefins is hence kinetically favorable. Using our calculated free energy barriers in Table 3 together with the data in Tables 1 and 2, we extended our kinetic model shown above such that we can simulate the entire reaction network. The results of such a kinetic simulation are shown in Fig. 5 for a temperature of 673.15 K with a feed of 1 bar of

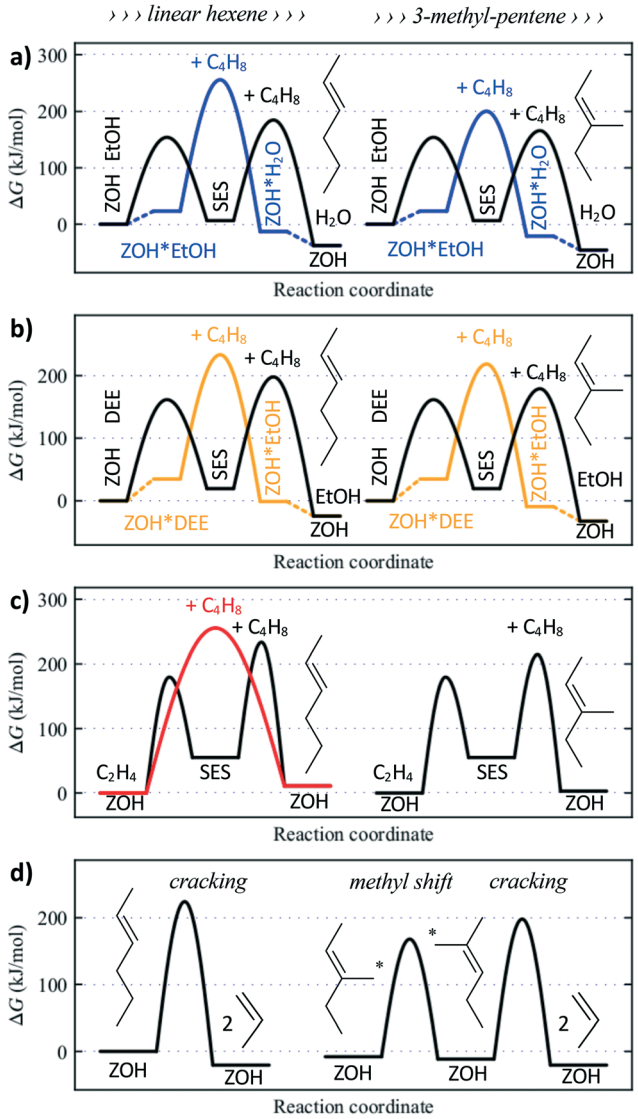


Fig. 4 Gibbs free energy diagram for the direct ethylations of butene at 673.15 K through a) EtOH (blue), b) DEE (orange) and c) ethene (red). Corresponding stepwise ethylations are shown in black. The formation of linear (left) and branched (right) hexene isomers can be compared. The barriers for a methyl shift and for propene formation through cracking are shown in d).

EtOH. As can be seen, the kinetic regimes can roughly be separated into three time domains. At 673.15 K, ethene is formed from EtOH within milliseconds (Fig. 5a). Ethene then dimerizes mediated by SES to form butene (Fig. 5b) on the scale of minutes, with the olefin partial pressures eventually approaching thermodynamic equilibrium through dimerization, ethylation and cracking (propene formation, Fig. 5c).

Note that branched hexene isomers are observed in small amounts while the partial pressure of linear hexene stays noticeably lower, which is due to the lower barriers for branched olefins (see Fig. 4 and 5). Due to the high temperatures, the equilibrium partial pressures of hexene isomers are always low and these species present intermediates towards propene. The propene formation accompanying the formation of hexene

Table 3 Elementary reaction steps for the formation, cracking and methyl shift reactions of hexene isomers with forward and backward free energy barriers at 673.15 K

| No. | Elementary reaction | | $\Delta G^{\ddagger}\left(\frac{\text{kJ}}{\text{mol}}\right)$ |
|---|---|---|---|
| 14 | ZOH*EtOH + butene | ⇄ZOH*$H_2O$ + hexene | 232, 268 |
| 15 | ZOH*EtOH + butene | ⇄ZOH*$H_2O$ + 3-Me–C5[a] | 177, 221 |
| 16 | SES + butene | ⇄ZOH + hexene | 178, 223 |
| 17 | SES + butene | ⇄ZOH + 3-Me–C5[a] | 159, 212 |
| 18 | ZOH*DEE + butene | ⇄ZOH*EtOH + hexene | 199, 235 |
| 19 | ZOH*DEE + butene | ⇄ZOH*EtOH + 3-Me–C5[a] | 184, 228 |
| 20 | ZOH + hexene | ⇄ZOH + ethene + butene | 245, 255 |
| 21 | ZOH + hexene | ⇄ZOH + 2 propene | 224, 245 |
| 22 | ZOH + 2-Me–C5[b] | ⇄ZOH + 2 propene | 210, 219 |
| 23 | ZOH + 2-Me–C5[b] | ⇄ZOH + 3-Me–C5[a] | 179, 176 |

[a] 3-Methyl-pentene. [b] 2-Methyl-pentene.

isomers is also within our expectations based on the computed barriers shown in Fig. 4. In this regard, the methyl shift of 3-methyl-pentene to 2-methyl-pentene and subsequent cracking to propene contributes most significantly to propene formation. From these Gibbs free energy diagrams it is also evident that the ethylation barriers for butene are lower than the ethylation barrier for ethene, similar to the trends of methylation barriers in the MTO process.[65]

Since odd-numbered olefins are eventually formed through cracking, the ETO process shows fairly similar product distributions compared to that observed for MTO.[8] Our findings hence support the work of Ingram and Lancashire who demonstrated that propene originates from cracking of presumably 2-methyl-pentene rather than from intermediate steps of butene formation.[39]

At lower temperatures, the formation of olefins higher than ethene quickly becomes unfeasible due to the high overall ethylation barriers. This is in line with experimental studies on H-ZSM-5 zeolite, where the selectivity for ethene formation was 95.5% at 543.15 K with almost no formation of higher olefins.[69] Only at temperatures above 573.15 K, significant amounts of higher olefins were observed, leading to gradually increased concentrations of butene and propene through cracking.[69] Although our calculations were performed for H-SSZ-13 and not H-ZSM-5, we have observed previously that significant differences in activation barriers are typically transferable to other zeolite frameworks.[63,70]

An analysis of the kinetics shows that the largest contributions come from reactions no. 2, 4, 7, 11, 17, 22 and 23 (see ESI†). Notably, the majority of the relevant reactions proceed *via* SES. This key aspect of the ETO process is analogous to that of the MTO process where most reactions of the olefin (and aromatic cycle) proceed *via* SMS under typical reaction conditions.

### 2.3 Correlations between ethylation and methylation

In the previous sections we noticed similarities between ETO and MTO in that the predominant alkylation pathways

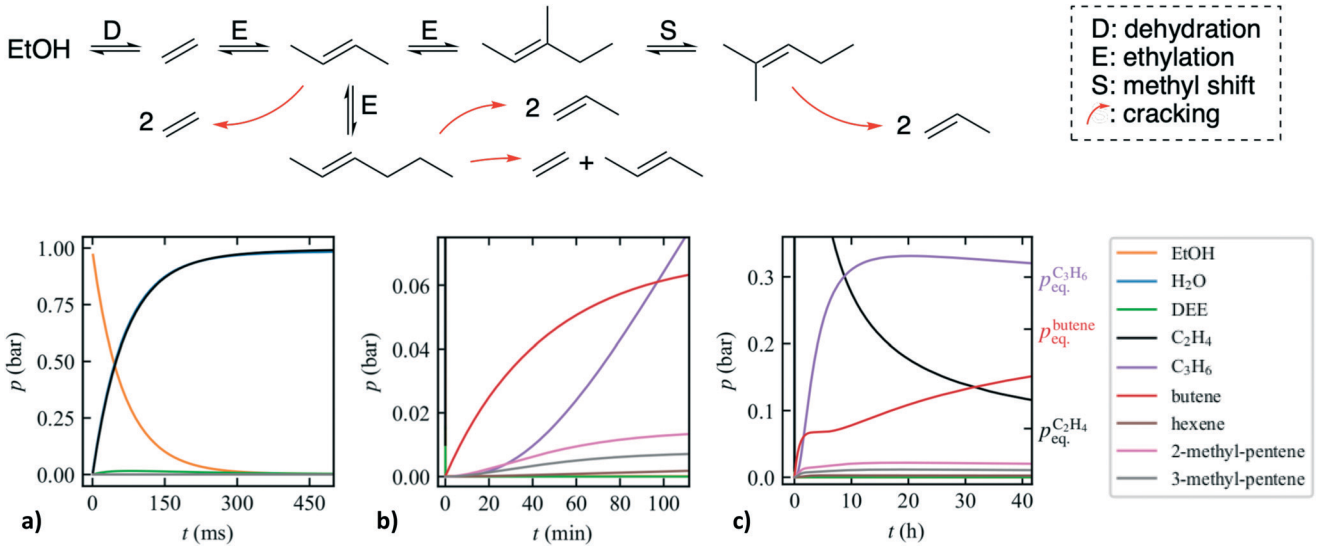


**Fig. 5** The upper mechanism is a subset of the ETO reaction network with even-numbered olefins (ethene, butene and hexene isomers). The even-numbered olefins are self-sustained by ethylations (*E*) unless hexene isomers are cracked to propene leading to the existence of odd-numbered olefins. The three diagrams depict the evolution of partial pressures in a corresponding kinetic simulation with the kinetic model combined from Tables 1–3 at 673.15 K with an initial pressure of 1 bar EtOH as a function of time. The crucial events happen on different time scales, namely (a) the conversion of EtOH to ethene within 300 ms, (b) the evolution of higher olefins with propene partial pressure surpassing butene after 97 min and (c) the slow equilibration that is not completed even after 40 h (equilibrium pressures are indicated). We note that further reactions of propene such as the formation of pentene through ethylation or the formation of heptene from propene and butene are not included in our simulation. Surface coverages are rather low at 673.15 K and thus not depicted here.

proceed *via* SAS. In the following, we compare free energy barriers for the second step of the stepwise alkylation, referenced to the gas phase, for a few olefin methylations and ethylations where we differentiate between linear and branched products. This correlation of intrinsic alkylation barriers for ETO and MTO at 673.15 K is presented in Fig. 6. As can be seen from Fig. 6, there is a correlation between methylation and ethylation barriers, with ethylation barriers being lower by about 11 kJ mol$^{-1}$.

In earlier work on MTO, we observed that the van-der-Waals (vdW) contribution to reaction barriers increases with decreasing zeolite pore size and that for H-SSZ-13 a contribution of roughly −5.8 kJ mol$^{-1}$ per adsorbate atom can be expected.[63] With the additional $CH_2$ fragment in ethylations, we would hence expect a vdW contribution to the energies of the barriers of about −17.4 kJ mol$^{-1}$. We indeed observe that the major part of the energetic differences of the reaction barriers (−8 kJ mol$^{-1}$) originates from the difference in vdW contributions (see Fig. S6 of the ESI†), albeit it is only half as strong as expected from earlier work. Since vdW interaction generally depends on the specific fitting of the adsorbate and the microporous structure, different zeolites can be expected to differ in their vdW interactions with adsorbates, although on average, interaction increases with the size of the adsorbate.[63,70]

## 3 Summary and conclusions

The formation of the HCP in the ETO process was studied based on batch reactor kinetics using *ab initio* calculated rate constants for the H-SSZ-13 catalyst. Temporary DEE formation with initially high DEE selectivity was observed within the first couple of minutes or seconds, at 473.15 K and 573.15 K, respectively, as long as the conversion was relatively low. This is due to the fact that at these

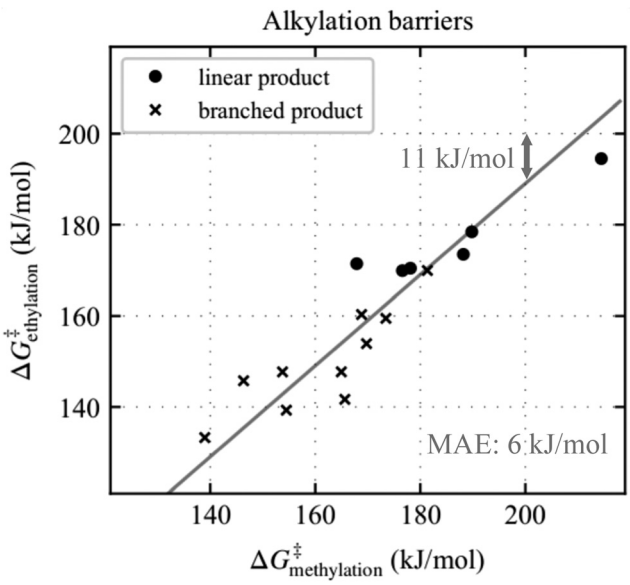


**Fig. 6** Correlation of free energy barriers, referenced to the gas phase, for the second step of the stepwise alkylation between ETO and MTO processes at 673.15 K and a reference pressure of 1 bar. The formation of linear and branched products is distinguished. The barriers for ethylation scale linearly with the barriers for methylation with a slope of one and an offset of 11 kJ mol$^{-1}$ with a mean absolute error (MAE) of 6 kJ mol$^{-1}$.

temperatures the dehydration pathway to DEE exhibits lower reaction barriers compared to the dehydration pathway to ethene. Ethene is formed rapidly at temperatures above 473.15 K with the main reaction pathway going through SES. Further ethylation to butene and hexene isomers, however, is significantly slower. Because butene ethylation is faster than ethene ethylation at 673.15 K, the ethylation of ethene to butene leads to the formation of hexene isomers opening cracking pathways to the formation of odd-numbered olefins (*i.e.* propene). Although the importance of cracking increases for higher olefins,[65] our simulations predict that propene is mainly formed through cracking of 2-methyl-pentene, a finding that has also been proposed based on experiments.[39] Furthermore, our study revealed a mechanistic similarity between ETO and MTO processes, that is the alkylation *via* SAS being favored over direct alkylation with the alkanol or alkylation through the dialkyl ether.

A correlation of Gibbs free energy barriers for alkylations mediated by SAS shows that ethylation barriers are generally lower than their methylation counterparts by roughly 11 kJ $mol^{-1}$, which we assign to differences in vdW interactions.

Our study thus provides theoretically derived reaction mechanisms for the dehydration of EtOH to ethene as well as further homologation and cracking steps.

# 4 Methods

We computed free energies as described in previous work.[55] A hexagonal unit cell with pre-optimized parameters ($a$ = 13.625 Å, $c$ = 15.067 Å) and one Brønsted acid site per unit cell was used for H-SSZ-13, see ESI† for locations of bulkier transition structures within the cavities. Structures were optimized employing periodic density functional theory (DFT) calculations with the dispersion-corrected PBE-D3[71,72] density functional (zero damping) using the VASP code with the standard PAWs[73–75] and an energy cutoff of 400 eV. A convergence criterion of 0.01 eV $Å^{-1}$ was applied to geometry optimizations. The Brillouin zone was sampled at the $\Gamma$-point only[76] using Gaussian smearing with a width of 0.1 eV. Transition structures were optimized using automated relaxed potential energy surface scans (ARPESS)[77] and the existence of one imaginary mode connecting the correct minima of the reaction was confirmed. Entropic contributions to the free energy barriers have been calculated using the harmonic approximation at the respective temperatures and at a reference pressure of 1 bar. Vibrational frequencies were derived from the partial Hessian matrix computed using a central finite difference scheme including only the adsorbate, the acid site and its adjacent Al- and Si-atom. Moreover, vibrational frequencies below 12 $cm^{-1}$ were raised to this value because they can lead to inaccurate entropies otherwise.[50] To obtain accurate reaction barriers,[59] corrections of the electronic energies according to eqn (1) and (2) were applied using a hierarchical cluster approach[78–83] (periodic models and 46T cluster models saturated by hydrogen atoms,[60] see ESI†) with highly accurate domain-based local pair natural orbital couple cluster (DLPNO-CCSD(T))[84–86] calculations combined with complete basis set (CBS) extrapolation based on DLPNO-MP2 calculations.

$$E = E^{\mathrm{PBC}}_{\mathrm{PBE\text{-}D3}} - E^{\mathrm{46T}}_{\mathrm{PBE\text{-}D3}} + E^{\mathrm{46T}}_{\mathrm{DLPNO\text{-}CCSD(T)/DZ}} + \Delta E^{\mathrm{46T}}_{\mathrm{MP2/CBS}} \quad (1)$$

$$\text{with } \Delta E^{\mathrm{46T}}_{\mathrm{MP2/CBS}} = E^{\mathrm{46T}}_{\mathrm{DLPNO\text{-}MP2/CBS}} - E^{\mathrm{46T}}_{\mathrm{DLPNO\text{-}MP2/DZ}} \quad (2)$$

In this approach, the cc-pVDZ basis set was used for $E^{\mathrm{46T}}_{\mathrm{DLPNO\text{-}CCSD(T)/DZ}}$ of the 46T cluster model, the def2-TZVPP basis set was used for $E^{\mathrm{46T}}_{\mathrm{PBE\text{-}D3}}$, and $\Delta E^{\mathrm{46T}}_{\mathrm{MP2/CBS}}$ stands for the difference between MP2-based CBS extrapolation ($E^{\mathrm{46T}}_{\mathrm{DLPNO\text{-}MP2/CBS}}$) and MP2/cc-pVDZ calculations for 46T clusters ($E^{\mathrm{46T}}_{\mathrm{DLPNO\text{-}MP2/DZ}}$). The CBS extrapolations of Hartree–Fock energies were carried out with the three-point exponential formula[87] with cc-pVXZ ($X$ = D, T, Q). For MP2-correlation, the two point $l^{-3}$ formula[88] was used with cc-pVXZ ($X$ = D, T). The non-periodic calculations were performed on 46T cluster models using the ORCA[89,90] and TURBOMOLE[91] program packages. PBE-D3 calculations on the 46T cluster models were performed using TURBOMOLE along with the def2-TZVPP basis set.[92,93] ORCA was used to perform DLPNO-CCSD(T),[86] DLPNO-MP2[94–96] and restricted Hartree–Fock (RHF) calculations for cc-pVXZ ($X$ = D, T, Q)[97] in the DLPNO approximation.[86,98–100] The RIJCOSX (resolution of identity for Coulomb integrals and semi-numerical chain-of-sphere integration for HF exchange integrals) approximation[101] with GridX6 was used in RHF calculations. Parts of the calculations were operated using the atomic simulation environment.[102]

The kinetic model comprises direct ethylations with DEE and EtOH, stepwise ethylations *via* SES as well as cracking reactions. Olefin isomerization barriers that only shift the double bond are expected to be small compared to ethylation and cracking barriers[65] and are therefore treated implicitly; *e.g.* 1-butene and 2-butene are lumped together as butene, 2-methyl-2-hexene is simply called 2-methyl-hexene, and so on. The kinetic simulations of the batch reactor were carried out based on the mean field approximation using simple Euler integration with a maximum time step smaller than $5 \times 10^{-7}$ s as implemented in the in-house code used in previous work.[13,14] Since we only consider the initial part of the ETO reaction mechanism we neglect diffusion limitations in the reactor simulations, thus assuming perfect mixing, as diffusion of smaller olefins has been shown to be rather fast.[103] We assume instantaneous equilibration of adsorption processes. For numerical reasons, the lower threshold of 80 kJ $mol^{-1}$ for adsorption barriers was set when deriving kinetic parameters from the barriers. It was verified that lowering this threshold has no impact on the outcome of the simulations (see ESI†). Further details on the kinetic model can be found in the ESI of our previous publication.[13]

# Author contributions

The manuscript was written through contributions of all authors. All authors have given approval to the final version of the manuscript.

## Conflicts of interest

There are no conflicts to declare.

## Acknowledgements

The authors gratefully acknowledge support by the GRK 2450, by the state of Baden-Württemberg through bwHPC (bwUniCluster and JUSTUS, RV bw17D01) and by the Helmholtz Association.

## Notes and references

1 G. A. Olah, *Angew. Chem., Int. Ed.*, 2013, **52**, 104–107.
2 V. F. Tret'yakov, Y. I. Makarfi, K. V. Tret'yakov, N. A. Frantsuzova and R. M. Talyshinskii, *Catal. Ind.*, 2010, **2**, 402–420.
3 M. R. Gogate, *Pet. Sci. Technol.*, 2019, **37**, 559–565.
4 I. M. Dahl and S. Kolboe, *Catal. Lett.*, 1993, **20**, 329–336.
5 I. Dahl and S. Kolboe, *J. Catal.*, 1994, **149**, 458–464.
6 I. M. Dahl and S. Kolboe, *J. Catal.*, 1996, **161**, 304–309.
7 D. S. Wragg, M. G. O'Brien, F. L. Bleken, M. Di Michiel, U. Olsbye and H. Fjellvåg, *Angew. Chem., Int. Ed.*, 2012, **51**, 7956–7959.
8 R. Johansson, S. L. Hruby, J. Rass-Hansen and C. H. Christensen, *Catal. Lett.*, 2009, **127**, 1–6.
9 U. Olsbye, S. Svelle, M. Bjørgen, P. Beato, T. V. W. Janssens, F. Joensen, S. Bordiga and K. P. Lillerud, *Angew. Chem., Int. Ed.*, 2012, **51**, 5810–5831.
10 A. D. Chowdhury, A. Lucini Paioni, G. T. Whiting, D. Fu, M. Baldus and B. M. Weckhuysen, *Angew. Chem., Int. Ed.*, 2019, **58**, 3908–3912.
11 W. Song, D. M. Marcus, H. Fu, J. O. Ehresmann and J. F. Haw, *J. Am. Chem. Soc.*, 2002, **124**, 3844–3845.
12 D. Lesthaeghe, V. Van Speybroeck, G. B. Marin and M. Waroquier, *Angew. Chem., Int. Ed.*, 2006, **45**, 1714–1719.
13 P. N. Plessow, A. Smith, S. Tischer and F. Studt, *J. Am. Chem. Soc.*, 2019, **141**, 5908–5915.
14 J. Amsler, P. N. Plessow and F. Studt, *Catal. Lett.*, 2021, **151**, 2595–2602.
15 N. Tajima, T. Tsuneda, F. Toyama and K. Hirao, *J. Am. Chem. Soc.*, 1998, **120**, 8222–8229.
16 A. D. Chowdhury, K. Houben, G. T. Whiting, M. Mokhtar, A. M. Asiri, S. A. Al-Thabaiti, S. N. Basahel, M. Baldus and B. M. Weckhuysen, *Angew. Chem., Int. Ed.*, 2016, **55**, 15840–15845.
17 Y. Liu, S. Müller, D. Berger, J. Jelic, K. Reuter, M. Tonigold, M. Sanchez-Sanchez and J. A. Lercher, *Angew. Chem., Int. Ed.*, 2016, **55**, 5723–5726.
18 X. Wu, S. Xu, W. Zhang, J. Huang, J. Li, B. Yu, Y. Wei and Z. Liu, *Angew. Chem., Int. Ed.*, 2017, **56**, 9039–9043.
19 K. Van der Borght, R. Batchu, V. V. Galvita, K. Alexopoulos, M.-F. Reyniers, J. W. Thybaut and G. B. Marin, *Angew. Chem., Int. Ed.*, 2016, **55**, 12817–12821.
20 R. H. Gil-Horán, J. C. Chavarría-Hernández, P. Quintana-Owen and A. Gutiérrez-Alejandre, *Top. Catal.*, 2020, **63**, 414–427.
21 X. Zhang, R. Wang, X. Yang and F. Zhang, *Microporous Mesoporous Mater.*, 2008, **116**, 210–215.
22 F. F. Madeira, N. Gnep, P. Magnoux, S. Maury and N. Cadran, *Appl. Catal., A*, 2009, **367**, 39–46.
23 C. P. Nash, A. Ramanathan, D. A. Ruddy, M. Behl, E. Gjersing, M. Griffin, H. Zhu, B. Subramaniam, J. A. Schaidle and J. E. Hensley, *Appl. Catal., A*, 2016, **510**, 110–124.
24 G. Garbarino, G. Pampararo, T. K. Phung, P. Riani and G. Busca, *Energies*, 2020, **13**, 3587.
25 M. Zhang and Y. Yu, *Ind. Eng. Chem. Res.*, 2013, **52**, 9505–9514.
26 K. Alexopoulos, M. John, K. Van der Borght, V. Galvita, M.-F. Reyniers and G. B. Marin, *J. Catal.*, 2016, **339**, 173–185.
27 M. E. Potter, L.-M. Armstrong and R. Raja, *Catal. Sci. Technol.*, 2018, **8**, 6163–6172.
28 H. Tong, *Petrochem. Technol.*, 1985, **14**, 92–93.
29 R. Le Van Mao, T. M. Nguyen and G. P. McLaughlin, *Appl. Catal.*, 1989, **48**, 265–277.
30 C. B. Phillips and R. Datta, *Ind. Eng. Chem. Res.*, 1997, **36**, 4466–4475.
31 L. Pan and H. Li, *Petrochem. Technol.*, 1985, **14**, 154–157.
32 L. Pan and H. Li, *Petrochem. Technol.*, 1987, **16**, 764–768.
33 D. Wang, J. Li and M. Fan, *Chin. J. Catal.*, 1992, **13**, 234–236.
34 T. Zhou, X.-X. Shi, L.-N. Wu, Q. Cui, H.-Y. Wang, Y. Hu and H. Huang, *J. Chem. Eng. Chin. Univ.*, 2011, **3**, 352–458.
35 H. Xin, X. Li, Y. Fang, X. Yi, W. Hu, Y. Chu, F. Zhang, A. Zheng, H. Zhang and X. Li, *J. Catal.*, 2014, **312**, 204–215.
36 T. K. Phung, L. Proietti Hernández, A. Lagazzo and G. Busca, *Appl. Catal., A*, 2015, **493**, 77–89.
37 D. Varisli, T. Dogu and G. Dogu, *Chem. Eng. Sci.*, 2007, **62**, 5349–5352.
38 Z. Benliang and Z. Baozhong, *Dongbei Shida Xuebao, Ziran Kexueban*, 1995, **1**, 70–72.
39 C. W. Ingram and R. J. Lancashire, *Catal. Lett.*, 1995, **31**, 395–403.
40 K. De Wispelaere, K. Hemelsoet, M. Waroquier and V. Van Speybroeck, *J. Catal.*, 2013, **305**, 76–80.
41 K. Hemelsoet, J. Van der Mynsbrugge, K. De Wispelaere, M. Waroquier and V. Van Speybroeck, *ChemPhysChem*, 2013, **14**, 1526–1545.
42 S. L. C. Moors, K. De Wispelaere, J. Van der Mynsbrugge, M. Waroquier and V. Van Speybroeck, *ACS Catal.*, 2013, **3**, 2556–2567.
43 C.-M. Wang, Y.-D. Wang and Z.-K. Xie, *J. Catal.*, 2013, **301**, 8–19.
44 C.-M. Wang, Y.-D. Wang and Z.-K. Xie, *Catal. Sci. Technol.*, 2014, **4**, 2631–2638.
45 V. Van Speybroeck, K. De Wispelaere, J. Van der Mynsbrugge, M. Vandichel, K. Hemelsoet and M. Waroquier, *Chem. Soc. Rev.*, 2014, **43**, 7326–7357.
46 C.-M. Wang, Y.-D. Wang, Y.-J. Du, G. Yang and Z.-K. Xie, *Catal. Sci. Technol.*, 2015, **5**, 4354–4364.
47 U. Olsbye, S. Svelle, K. P. Lillerud, Z. H. Wei, Y. Y. Chen, J. F. Li, J. G. Wang and W. B. Fan, *Chem. Soc. Rev.*, 2015, **44**, 7155–7176.

48 M. DeLuca, P. Kravchenko, A. Hoffman and D. Hibbitts, *ACS Catal.*, 2019, **9**, 6444–6460.
49 M. DeLuca, C. Janes and D. Hibbitts, *ACS Catal.*, 2020, **10**, 4593–4607.
50 R. Y. Brogaard, R. Henry, Y. Schuurman, A. J. Medford, P. G. Moses, P. Beato, S. Svelle, J. K. Nørskov and U. Olsbye, *J. Catal.*, 2014, **314**, 159–169.
51 A. Ghorbanpour, J. D. Rimer and L. C. Grabow, *ACS Catal.*, 2016, **6**, 2287–2298.
52 I. Yarulina, A. D. Chowdhury, F. Meirer, B. M. Weckhuysen and J. Gascon, *Nat. Catal.*, 2018, **1**, 398–411.
53 A. D. Chowdhury, A. L. Paioni, K. Houben, G. T. Whiting, M. Baldus and B. M. Weckhuysen, *Angew. Chem., Int. Ed.*, 2018, **57**, 8095–8099.
54 A. A. Arvidsson, P. N. Plessow, F. Studt and A. Hellman, *J. Phys. Chem. C*, 2020, **124**, 14658–14663.
55 M. Fečík, P. N. Plessow and F. Studt, *Catal. Sci. Technol.*, 2021, **11**, 3826–3833.
56 M. John, K. Alexopoulos, M.-F. Reyniers and G. B. Marin, *ACS Catal.*, 2016, **6**, 4081–4094.
57 M. Fečík, P. N. Plessow and F. Studt, *J. Phys. Chem. C*, 2018, **122**, 23062–23067.
58 A. J. Hoffman, J. S. Bates, J. R. Di Iorio, S. V. Nystrom, C. T. Nimlos, R. Gounder and D. Hibbitts, *Angew. Chem.*, 2020, **132**, 18845–18853.
59 T. J. Goncalves, P. N. Plessow and F. Studt, *ChemCatChem*, 2019, **11**, 4368–4376.
60 P. N. Plessow and F. Studt, *ACS Catal.*, 2017, **7**, 7987–7994.
61 M. Fečík, P. N. Plessow and F. Studt, *ACS Catal.*, 2020, **10**, 8916–8925.
62 D. Zhang, R. Wang and X. Yang, *Catal. Lett.*, 2008, **124**, 384–391.
63 P. N. Plessow and F. Studt, *Catal. Lett.*, 2018, **148**, 1246–1253.
64 F. Bleken, M. Bjørgen, L. Palumbo, S. Bordiga, S. Svelle, K.-P. Lillerud and U. Olsbye, *Top. Catal.*, 2009, **52**, 218–228.
65 P. N. Plessow and F. Studt, *Catal. Sci. Technol.*, 2018, **8**, 4420–4429.
66 S. Namuangruk, P. Pantu and J. Limtrakul, *ChemPhysChem*, 2005, **6**, 1333–1339.
67 C. Liu, I. Tranca, R. A. van Santen, E. J. M. Hensen and E. A. Pidko, *J. Phys. Chem. C*, 2017, **121**, 23520–23530.
68 C.-M. Wang, Y.-D. Wang and Z.-K. Xie, *Catal. Sci. Technol.*, 2019, **9**, 2245–2252.
69 J. Lu and Y. Liu, *J. Nat. Gas Chem.*, 2011, **20**, 162–166.
70 M. Fečík, P. N. Plessow and F. Studt, *ChemCatChem*, 2021, **13**, 2451–2458.
71 J. P. Perdew, K. Burke and M. Ernzerhof, *Phys. Rev. Lett.*, 1996, **77**, 3865–3868.
72 S. Grimme, J. Antony, S. Ehrlich and H. Krieg, *J. Chem. Phys.*, 2010, **132**, 154104.
73 P. E. Blöchl, *Phys. Rev. B: Condens. Matter Mater. Phys.*, 1994, **50**, 17953–17979.
74 G. Kresse and J. Furthmüller, *Phys. Rev. B: Condens. Matter Mater. Phys.*, 1996, **54**, 11169–11186.
75 G. Kresse and D. Joubert, *Phys. Rev. B: Condens. Matter Mater. Phys.*, 1999, **59**, 1758–1775.
76 H. J. Monkhorst and J. D. Pack, *Phys. Rev. B: Solid State*, 1976, **13**, 5188–5192.
77 P. N. Plessow, *J. Chem. Theory Comput.*, 2018, **14**, 981–990.
78 C. Tuma and J. Sauer, *Phys. Chem. Chem. Phys.*, 2006, **8**, 3955–3965.
79 C. Tuma, T. Kerber and J. Sauer, *Angew. Chem., Int. Ed.*, 2010, **49**, 4678–4680.
80 S. Svelle, C. Tuma, X. Rozanska, T. Kerber and J. Sauer, *J. Am. Chem. Soc.*, 2009, **131**, 816–825.
81 N. Hansen, T. Kerber, J. Sauer, A. T. Bell and F. J. Keil, *J. Am. Chem. Soc.*, 2010, **132**, 11525–11538.
82 M. Rybicki and J. Sauer, *J. Am. Chem. Soc.*, 2018, **140**, 18151–18161.
83 Q. Ren, M. Rybicki and J. Sauer, *J. Phys. Chem. C*, 2020, **124**, 10067–10078.
84 C. Riplinger and F. Neese, *J. Chem. Phys.*, 2013, **138**, 034106.
85 C. Riplinger, B. Sandhoefer, A. Hansen and F. Neese, *J. Chem. Phys.*, 2013, **139**, 134101.
86 C. Riplinger, P. Pinski, U. Becker, E. F. Valeev and F. Neese, *J. Chem. Phys.*, 2016, **144**, 024109.
87 D. Feller, *J. Chem. Phys.*, 1992, **96**, 6104–6114.
88 T. Helgaker, W. Klopper, H. Koch and J. Noga, *J. Chem. Phys.*, 1997, **106**, 9639–9646.
89 F. Neese, *Wiley Interdiscip. Rev.: Comput. Mol. Sci.*, 2012, **2**, 73–78.
90 F. Neese, *WIREs Comput. Mol. Sci.*, 2018, **8**, e1327.
91 TURBOMOLE V.7.1 2016, a Development of Karlsruhe Institute of Technology, Karlsruhe, 1989–2019, TURBOMOLE GmbH, since 2007; Available from **https://www.turbomole.com**, Turbomole GmbH, 2016.
92 F. Weigend, F. Furche and R. Ahlrichs, *J. Chem. Phys.*, 2003, **119**, 12753–12762.
93 F. Weigend and R. Ahlrichs, *Phys. Chem. Chem. Phys.*, 2005, **7**, 3297.
94 C. L. Janssen and I. M. Nielsen, *Chem. Phys. Lett.*, 1998, **290**, 423–430.
95 W. Jiang, N. J. DeYonker and A. K. Wilson, *J. Chem. Theory Comput.*, 2012, **8**, 460–468.
96 F. Weigend, M. Häser, H. Patzelt and R. Ahlrichs, *Chem. Phys. Lett.*, 1998, **294**, 143–152.
97 T. H. Dunning, *J. Chem. Phys.*, 1989, **90**, 1007–1023.
98 Y. Minenkov, E. Chermak and L. Cavallo, *J. Chem. Theory Comput.*, 2015, **11**, 4664–4676.
99 Y. Minenkov, G. Bistoni, C. Riplinger, A. A. Auer, F. Neese and L. Cavallo, *Phys. Chem. Chem. Phys.*, 2017, **19**, 9374–9391.
100 M. Saitow, U. Becker, C. Riplinger, E. F. Valeev and F. Neese, *J. Chem. Phys.*, 2017, **146**, 164105.
101 F. Neese, F. Wennmohs, A. Hansen and U. Becker, *Chem. Phys.*, 2009, **356**, 98–109.
102 A. Hjorth Larsen, J. Jørgen Mortensen, J. Blomqvist, I. E. Castelli, R. Christensen, M. Dułak, J. Friis, M. N. Groves, B. Hammer, C. Hargus, E. D. Hermes, P. C. Jennings, P. Bjerre Jensen, J. Kermode, J. R. Kitchin, E. Leonhard Kolsbjerg, J. Kubal, K. Kaasbjerg, S. Lysgaard, J. Bergmann Maronsson, T. Maxson, T. Olsen, L. Pastewka, A. Peterson, C. Rostgaard, J. Schiøtz, O. Schütt, M. Strange, K. S. Thygesen, T. Vegge,

L. Vilhelmsen, M. Walter, Z. Zeng and K. W. Jacobsen, *J. Phys.: Condens. Matter*, 2017, **29**, 273002.

103 A. T. Smith, P. N. Plessow and F. Studt, *Chem. Phys.*, 2021, **541**, 111033.